Engineering Analysis with Boundary Elements 70 (2016) 1–11

Contents lists available at ScienceDirect

Engineering Analysis with Boundary Elements

journal homepage: www.elsevier.com/locate/enganabound

Free and forced vibration analyses using the four-node quadrilateral element with continuous nodal stress

Yongtao Yang [a], Li Chen [a,*], Dongdong Xu [b], Hong Zheng [a]

[a] State Key Laboratory of Geomechanics and Geotechnical Engineering, Institute of Rock and Soil Mechanics, Chinese Academy of Sciences, Wuhan, China
[b] Key Laboratory of Geotechnical Mechanics and Engineering of Ministry of Water Resources, Yangtze River Scientific Research Institute, Wuhan, China

ARTICLE INFO

Article history:
Received 28 September 2015
Received in revised form
27 March 2016
Accepted 17 May 2016

Keywords:
Partition of unity method
'FE-Meshfree' element
Quad4-CNS
Mesh distortion
Free and forced vibration analyses

ABSTRACT

The recently published four-node quadrilateral element with continuous nodal stress (Quad4-CNS) is extended to free and forced vibration analyses of two-dimensional solids. The Quad4-CNS element can be regarded as a partition-of-unity (PU) based 'FE-Meshfree' element which inherits better accuracy, higher convergence rate, and high tolerance to mesh distortion from the meshfree methods, while preserving the Kronecker-delta property of the finite element method (FEM). Moreover, the Quad4-CNS element is free from the linear dependence problem which otherwise cripples many of the PU based finite elements. Several free and forced vibration problems are solved and the performance of the element is compared with that of the four-node isoparametric quadrilateral element (Quad4) and eight-node isoparametric quadrilateral element (Quad8). The results show that, for regular meshes, the performance of the element is superior to that of Quad4 element, and comparable to that of Quad8 element. For distorted meshes, the present element has better mesh-distortion tolerance than Quad4 and Quad8 elements.

1. Introduction

In the past several decades, the finite element method (FEM) [1] has been extensively used in many fields of engineering [2–4]. Nevertheless, accuracy of some classic isoparametric elements is highly sensitive to mesh distortions [5]. Recently, the meshfree or meshless methods (MMs) which do not need a mesh to discretize the problem domain and therefore are not limited by mesh distortion woes [6], have attracted many researchers. The meshfree methods are very suitable to solve practical problems including large deformation [7] and fracture propagation [8]. Some of the important works associated with meshfree methods are Smoothed Particle Hydrodynamics (SPH) [9], Diffuse Element Method (DEM) [10], Element-Free Galerkin method (EFG) [11], reproducing kernel particle method (RKPM) [12], stable particle methods [13], meshfree local Petrov-Galerkin method (MLPG) [14], point interpolation method (PIM) [15], radial point interpolation method (RPIM) [16] and smoothed point interpolation methods [17]. Like FEM, the meshfree methods either are not free from drawbacks [6]. Shape functions in some of the meshfree methods do not possess the much desired Kronecker delta property which renders the application of boundary condition more difficult than in FEM. The meshfree methods are also computationally more expensive than FEM [6]. As a result, some hybrid schemes [18] have been proposed to improve the properties of meshfree methods.

In recent years, Partition-of-unity (PU) based methods [19] have been developed and successfully used in many fields [20–23]. Notable among these PU based methods are hp-clouds [24], generalized finite element method (GFEM) [25], particle-partition of unity method [26], numerical manifold method [27–31] and extended finite element method (XFEM) [32]. An attractive feature of PU-based methods is that they are capable of constructing a higher order global approximation by simply increasing the order of the local approximation functions without adding new nodes [33]. However, "linear dependence" (LD) problem occurs when both the PU functions and the local functions are taken as explicit polynomials [6,19]. Here, the "linear dependence" (LD) problem means after applying the basic boundary condition to eliminate the rigid body displacement, the global stiffness matrix is still singular. Some effective approaches to eliminate the LD problems can be found in [34,35]. In other front, Liu and his co-workers have developed a family of smoothed finite element methods (S-FEMs), such as cell-based S-FEM (CS-FEM) [36], node-based S-FEM (NS-FEM) [37], edge-based S-FEM (ES-FEM) [38], and face-based S-FEM (FS-FEM) [39] to improve FEM. Thanks to the smoothing technique [40], the S-FEM has "softer" stiffness than FEM, and yields more accurate solutions [36].

In order to synergize the individual strengths of meshfree and

* Corresponding author.
E-mail address: lchen1990geoengineer@gmail.com (L. Chen).

http://dx.doi.org/10.1016/j.enganabound.2016.05.005
0955-7997/

finite element methods, Rajendran et al. developed a new family of PU-based [19] 'FE-Meshfree' elements [6,33,41] for linear, geometry nonlinear and free vibration analyses. 'FE-Meshfree' elements combine the classical shape functions of isoparametric elements with the shape functions of a meshfree method so as to arrive at hybrid shape functions termed as *composite shape functions* [33]. As a result, these 'FE-Meshfree' elements inherit better accuracy, higher convergence rate, and high tolerance to mesh distortion from the meshfree methods, while preserving the Kronecker-delta property of the standard isoparametric elements. Moreover, these 'FE-Meshfree' elements have been known to be free from the linear dependence problem which otherwise cripples many of the PU-based finite elements [6]. Although 'FE-Meshfree' elements can construct higher order shape functions than classical isoparametric elements, derivatives of *composite shape functions* of 'FE-Meshfree' elements [6,33,41,42] are not continuous at nodes and extra smoothing operations are required to calculate nodal stress in post processing. To further improve the property of 'FE-Meshfree' elements, Tang et al. [43] developed a new hybrid 'FE-Meshfree' four-node quadrilateral element with continuous nodal stress (Quad4-CNS). Furthermore, a hybrid 'FE-Meshfree' three-node triangular element with continuous nodal stress (Trig3-CNS) [44] was developed. These two elements have been successfully used for linear elasticity problems [43,44].

In the present paper, the Quad4-CNS element is extended to free and forced vibration analyses of two dimensional solids. The outline of this paper is as follows. Section 2 briefly reviews the construction of shape functions for the Quad4-CNS element. Section 3 gives the equations for free and forced vibration analyses. Typical numerical tests are carried out to assess accuracy of the proposed Quad4-CNS element in Section 4. Finally, conclusions are drawn in Section 5.

2. Construction shape function for Quad4-CNS

Consider a quadrilateral domain Ω described by four nodes $\{P_1\ P_2\ P_3\ P_4\}$ and introduce an arbitrary point $P(\boldsymbol{x})$ with the coordinates $\boldsymbol{x}=(x, y)$. According to the concept of PUM [19], in the quadrilateral domain Ω, the Quad4-CNS global approximation $u^h(\boldsymbol{x})$ can be represented in the following form:

$$u^h(\boldsymbol{x}) = w_1(\boldsymbol{x})u_1(\boldsymbol{x}) + w_2(\boldsymbol{x})u_2(\boldsymbol{x}) + w_3(\boldsymbol{x})u_3(\boldsymbol{x}) + w_4(\boldsymbol{x})u_4(\boldsymbol{x}) \tag{1}$$

where, $w_i(\boldsymbol{x})$ and $u_i(\boldsymbol{x})$ are the weight functions and the nodal approximations associated with node i.

The weight functions $\{w_i(\boldsymbol{x}), i = 1, 2, 3, 4\}$ with the global Cartesian coordinates are mapped from 'parent' weight functions in the local coordinates [43]. The formulations for coordinate transformation are represented as:

$$x = \tilde{N}_1(\xi, \eta)x_1 + \tilde{N}_2(\xi, \eta)x_2 + \tilde{N}_3(\xi, \eta)x_3 + \tilde{N}_4(\xi, \eta)x_4 \tag{2}$$

$$y = \tilde{N}_1(\xi, \eta)y_1 + \tilde{N}_2(\xi, \eta)y_2 + \tilde{N}_3(\xi, \eta)y_3 + \tilde{N}_4(\xi, \eta)y_4 \tag{3}$$

where $\tilde{N}_1(\xi, \eta)$, $\tilde{N}_2(\xi, \eta)$, $\tilde{N}_3(\xi, \eta)$, $\tilde{N}_4(\xi, \eta)$ are expressed in the following form [1]

$$\tilde{N}_i(\xi, \eta) = (1 + \xi_0)(1 + \eta_0)/4, \xi_0 = \xi_i\xi, \quad \eta_0 = \eta_i\eta, \ i = 1, 2, 3, 4. \tag{4}$$

Unlike the 'FE-Meshfree' QUAD4 element with least square point interpolation functions (Quad4-LSPIM) [41], which uses the shape functions of Quad4 to define its weight functions, the weight functions of Quad4-CNS element are written as [43]

$$w_i(\xi, \eta) = (1 + \xi_0)(1 + \eta_0)(2 + \xi_0 + \eta_0 - \xi^2 - \eta^2)/8, i = 1, 2, 3, 4. \tag{5}$$

There are three important features for the weight functions of Quad4-CNS element as described in Appendix A.

The nodal approximations associated with node i, as yet unknown, are expressed in the interpolation form as

$$u_i(\boldsymbol{x}) = \sum_{j=1}^{n^{[i]}} \hat{\phi}_j^{[i]}(\boldsymbol{x})a_j, \tag{6}$$

in which $n^{[i]}$ is the total number of nodes in the domain Ω_i, (Fig. B1), a_j is the nodal displacement of node j and $\hat{\phi}_j^{[i]}(\boldsymbol{x})$ is the shape function of the nodal approximation $u_i(\boldsymbol{x})$ associated with node j. (The procedure to obtain u_i is described in Appendix B.)

The Quad4-CNS approximation $u^h(\boldsymbol{x})$ can be represented in a common form:

$$u^h(\boldsymbol{x}) = \sum_{i=1}^{N} \phi_i(\boldsymbol{x})a_i, \tag{7}$$

in which $\phi_i(\boldsymbol{x})$ is the shape function corresponding to the node i. N is the total number of the nodes in domain $\hat{\Omega}$ (Fig. B2). Substitution of Eq. (6) into Eq. (1), and then the Quad4-CNS global approximation can be constructed as

$$u^h(\boldsymbol{x}) = \sum_{i=1}^{4} w_i(\boldsymbol{x}) \sum_{j=1}^{n^{[i]}} \hat{\phi}_j^{[i]}(\boldsymbol{x})a_j. \tag{8}$$

By manipulating Eq. (8), the Quad4-CNS shape functions in Eq. (7) can be represented as

$$\phi_i(\boldsymbol{x}) = w_1(\boldsymbol{x})\hat{\phi}_i^{[1]}(\boldsymbol{x}) + w_2(\boldsymbol{x})\hat{\phi}_i^{[2]}(\boldsymbol{x}) + w_3(\boldsymbol{x})\hat{\phi}_i^{[3]}(\boldsymbol{x}) + w_4(\boldsymbol{x})\hat{\phi}_i^{[4]}(\boldsymbol{x}) \tag{9}$$

If node j is not in the neighboring domain Ω_i, then $\hat{\phi}_j^{[i]}(\boldsymbol{x})$ is defined to be of zero value,

$$\hat{\phi}_j^{[i]}(\boldsymbol{x}) \equiv 0. \tag{10}$$

Some useful properties of Quad4-CNS are shown as follows [43]:

(1) The derivative of weight function is of zero value at the nodes.
(2) The derivative of Quad4-CNS global approximation is continuous at the nodes.
(3) The Kronecker-delta property

$$\phi_i(\boldsymbol{x}_j) = \delta_{ij} \tag{11}$$

3. Forced and free vibration analyses

Consider a 2D problem defined in domain V and let domain V be discretized by a set of non-overlapping quadrilateral domain: $V = \cup_{i=1}^{N} V_i$. Using the Quad4-CNS shape functions derived in Section 2, the discretized equation system of dynamic analysis is obtained as [16,38]

$$\mathbf{M}\ddot{\mathbf{a}} + \mathbf{C}\dot{\mathbf{a}} + \mathbf{K}\mathbf{a} = \mathbf{f} \tag{12}$$

where $\mathbf{K}$, and $\mathbf{M}$ are the global stiffness matrix and global mass matrix, respectively, and defined by

$$\mathbf{K}_{ij} = \sum \mathbf{K}_{ij}^e, \ \mathbf{M}_{ij} = \sum \mathbf{M}_{ij}^e \tag{13}$$

where

$$\mathbf{K}_{ij}^{e} = \int_{V_k} \mathbf{B}_i^{\mathrm{T}} \mathbf{D} \mathbf{B}_j d\Omega \tag{14}$$

$$\mathbf{M}_{ij}^{e} = \int_{V_k} \rho \boldsymbol{\phi}_i^{\mathrm{T}} \boldsymbol{\phi}_j d\Omega \tag{15}$$

$$\mathbf{B}_i = \begin{bmatrix} \frac{\partial \phi_i}{\partial x} & 0 & \frac{\partial \phi_i}{\partial y} \\ 0 & \frac{\partial \phi_i}{\partial y} & \frac{\partial \phi_i}{\partial x} \end{bmatrix}^{\mathrm{T}} \tag{16}$$

$$\boldsymbol{\varphi}_i = \begin{bmatrix} \phi_i & 0 \\ 0 & \phi_i \end{bmatrix}^{\mathrm{T}} \tag{17}$$

D is the matrix of material constants.

For simplicity of implementation, the Rayleigh damping is used, and the damping matrix **C** is assumed to be a linear combination of **K** and **M**,

$$\mathbf{C} = \beta_1 \mathbf{M} + \beta_2 \mathbf{K} \tag{18}$$

where β_1 and β_2 are the Rayleigh damping coefficients.

To solve the second-order time dependent problems, many method such as the Newmark method and Crank–Nicholson method [1] have been proposed. In this study, the Newmark method is used. When the state at t is known, the new state at $t + \Delta t$ can be calculated using the following formulations:

$$\left(\mathbf{K} + \frac{1}{\alpha \Delta t^2}\mathbf{M} + \frac{\delta}{\alpha \Delta t}\mathbf{C}\right)\mathbf{a}_{t+\Delta t} = \mathbf{f}_{t+\Delta t} + \mathbf{M}\left[\frac{1}{\alpha \Delta t^2}\mathbf{a}_t + \frac{1}{\alpha \Delta t}\dot{\mathbf{a}}_t + \left(\frac{1}{2\alpha} - 1\right)\ddot{\mathbf{a}}_t\right] + \mathbf{C}\left[\frac{\delta}{\alpha \Delta t}\mathbf{a}_t + \left(\frac{\delta}{\alpha} - 1\right)\dot{\mathbf{a}}_t + \left(\frac{\delta}{2\alpha} - 1\right)\Delta t\left(\frac{1}{2\alpha} - 1\right)\ddot{\mathbf{a}}_t\right] \tag{19}$$

$$\ddot{\mathbf{a}}_{t+\Delta t} = \frac{1}{\alpha \Delta t^2}(\mathbf{a}_{t+\Delta t} - \mathbf{a}_t) - \frac{1}{\alpha \Delta t}\dot{\mathbf{a}}_t - \left(\frac{1}{2\alpha} - 1\right)\ddot{\mathbf{a}}_t \tag{20}$$

$$\dot{\mathbf{a}}_{t+\Delta t} = \dot{\mathbf{a}}_t + \Delta t(1 - \delta)\ddot{\mathbf{a}}_t + \delta \Delta t \ddot{\mathbf{a}}_{t+\Delta t} \tag{21}$$

Without damping and forcing terms, Eq. (12) will reduce to a homogenous equation:

$$\mathbf{M}\ddot{\mathbf{a}} + \mathbf{K}\mathbf{a} = \mathbf{0} \tag{22}$$

A general solution of Eq. (22) can be written as

$$\mathbf{a} = \bar{\mathbf{a}}\, exp(i\omega t) \tag{23}$$

where t denotes time. $\bar{\mathbf{a}}$ is the eigenvector and ω is natural frequency.

Substitution Eq. (23) into Eq. (22), the natural frequency ω can be found by solving the following eigenvalue equation:

$$K\bar{\mathbf{a}} - \lambda M\bar{\mathbf{a}} = \mathbf{0},\ \lambda = \omega^2, \tag{24}$$

4. Numerical examples

Numerical tests with the present Quad4-CNS element for free vibration analyses of 2-D solids were carried out. Except specially mentioned, the physical units used in the present work are based on the international standard unit system. Here, n defines the total number of the nodes in the computational model. To assess accuracy and convergence, the relative error in the natural frequency is defined, as follows:

$$Re = \frac{\omega^{num} - \omega^{ref}}{\omega^{ref}}, \tag{25}$$

where the superscript "ref" represents the reference solution and the superscript "num" denotes a numerical solution.

4.1. Comparison of shape functions

The shape functions of 3-node triangular element (Trig3), Quad4, 6-node triangular element (Trig6), Quad8 and Quad4-CNS are compared in Fig. 1. It is observed that the derivative of Quad4-CNS shape functions is continuous at the node. However, the derivatives of shape functions for Trig3, Quad4, Trig6 and Quad8 elements are not continuous at the nodes. The shape function of Quad4-CNS elements is smoother than that of Trig3, Quad4, Trig6 and Quad8 elements on edges of elements.

4.2. A cantilever beam

A two dimensional cantilever beam fixed at the left end with length L and height D is studied for the various behaviors of Quad4-CNS element as a benchmark problem, as shown in Fig. 2. The parameters in the computation are taken as $L=100$ mm, $D=10$ mm, Young's modulus $E=2.1\times10^4$ kg f/mm^2, Poisson's ratio $\nu=0.3$, thickness $t=1$ mm, mass density $\rho=8.0\times10^{-10}$ kg fs^2/mm^4. This problem has earlier been analyzed by Liu and Gu [16] using a local radial point interpolation method (LRPIM) with the multi-quadrics (MQ) radial function and Gaussian radial function, by Nagashima [45] using the node-by-node meshless (NBNM) method and by Liu and Nguyen-Thoi using node-based S-FEM with triangular mesh (NS-FEM-T3) and edge-based S-FEM with triangular mesh (ES-FEM-T3) [36,38]. The results obtained using the present Quad4-CNS element are compared with those of NS-FEM-T3 [36], ES-FEM-T3 [38], Quad4, Quad8, Trig3 and 6-node triangular element (Trig6).

4.2.1. Convergence study

To examine the convergence of numerical solutions in Quad4-CNS element, three discrete models with regular grids are constructed as shown in Fig. 3. The frequencies computed for the three meshes are listed in Tables 1–3. The reference results shown in last column of Tables 1–3 were proposed by Liu and Gu [16]. Fig. 4 shows the plot of error in the first two natural frequencies obtained using the present Quad4-CNS element as well as Quad4, NS-FEM-T3 [36] and ES-FEM-T3 [38]. It is seen that the error in the first two natural frequencies given by Quad4-CNS element is generally less than that given by Quad4 element, NS-FEM-T3 and ES-FEM-T3. The results obtained from the present Quad4-CNS element also exhibit a faster convergence than those elements including Quad4, NS-FEM-T3 and ES-FEM-T3. Even for the coarse mesh, the results given by Quad4-CNS element are close to the reference solution.

The first 10 eigenmodes, obtained with the Quad4-CNS element using the Mesh B (Fig. 3(b)) are plotted in Fig. 5. These modeshape plots compare well with that of ES-FEM-T3 [38].

4.2.2. Sensitivity to distorted meshes

As shown in Fig. 6, two distorted meshes are used to examine the influence of the mesh quality. The result obtained with six element types viz., Trig3, Trig6, Quad4, Quad8 and the present Quad4-CNS, are shown in Table 4 and 5, respectively. It is seen that accuracy given by the present Quad4-CNS element is generally better than that given by Trig3 and Quad4 elements, and comparable to that given by Trig6 and Quad8 elements. Even for the

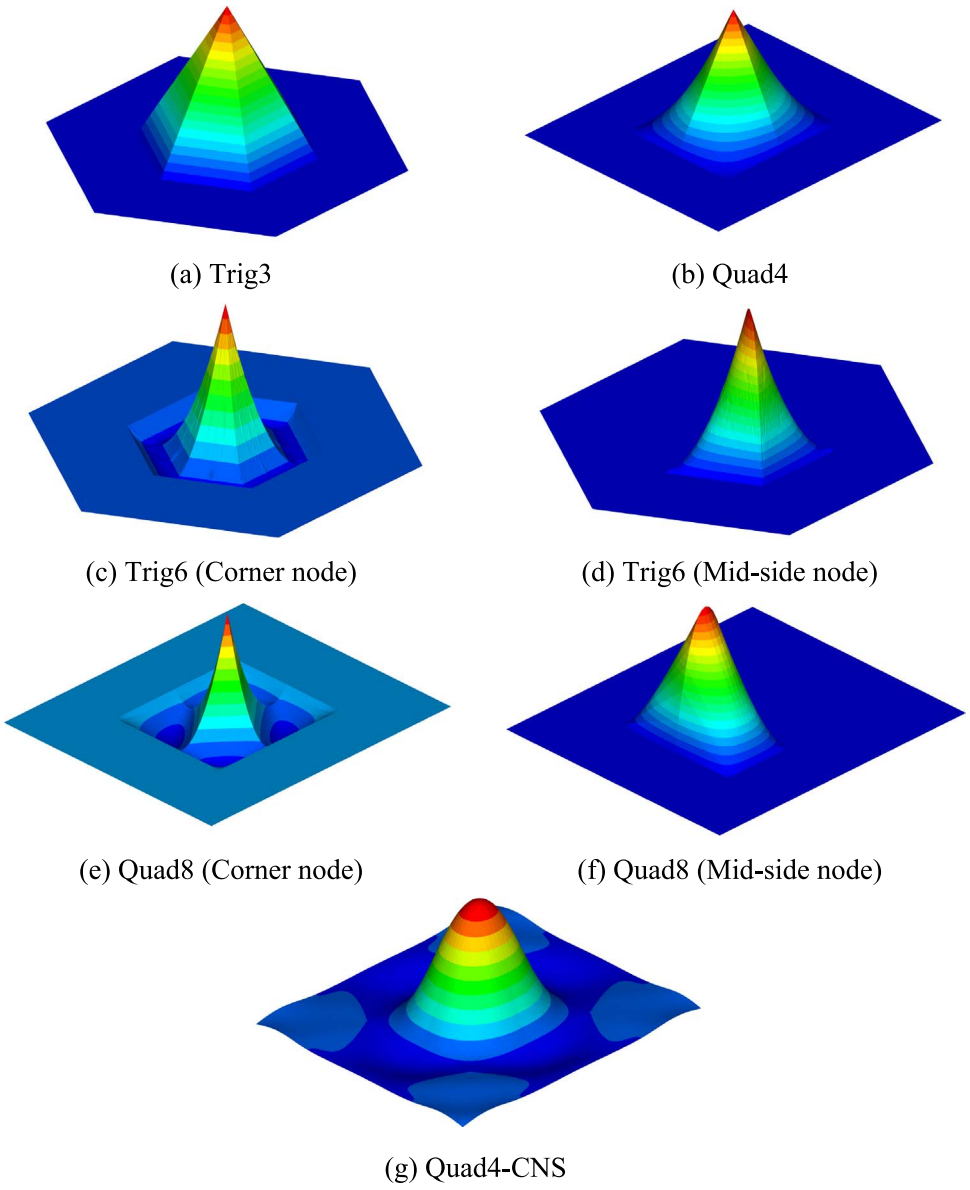

Fig. 1. Comparison of the shape functions of Trig3, Quad4, Trig6, Quad8 and Quad4-CNS (the Quad4-CNS shape function is C^1 continuous at the nodes).

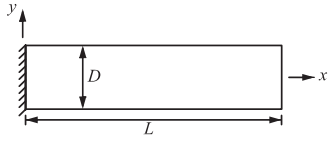

Fig. 2. Free vibration analysis of a 2D cantilever beam.

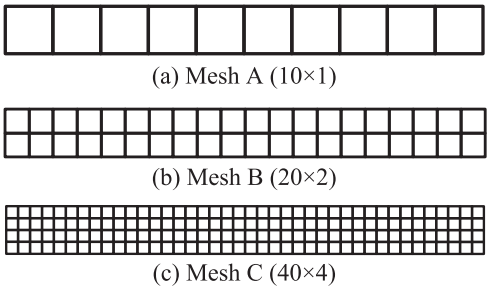

Fig. 3. Regular mesh for cantilever beam in Fig. 2.

Table 1
Comparison of computed frequencies (Hz) for the cantilever beam with Mesh A (10 × 1).

Mode	Quad4 (22 nodes, 10 elements)	NS-FEM-T3 [36] (22 nodes, 20 elements)	ES-FEM-T3 [38] (22 nodes, 20 elements)	Quad4-CNS (22 nodes, 10 elements)	Reference [16]
1	1000	580	1050	871	823
2	6077	3240	6020	5512	4937
3	12,863	7440	12,830	12,842	12,824
4	16,423	9880	15,180	15,555	13,005
5	30,962	10,110	26,360	31,146	23,632
6	38,921	11,350	37,720	38,583	36,040
7	49,339	12,780	38,560	54,202	38,442
8	65,982	15,710	50,350	64,975	49,616
9	71,244	23,700	60,830	87,127	63,955
10	94,728	32,690	61,520	93,668	63,967

distorted mesh, very good results are obtained using the Quad4-CNS element. This is a very significant advantage of Quad4-CNS element. This property is very beneficial for practical applications

Table 2
Comparison of computed frequencies (Hz) for the cantilever beam with Mesh B (20×2).

Mode	Quad4 (63 nodes, 40 elements)	NS-FEM-T3 [36] (63 nodes, 80 elements)	ES-FEM-T3 [38] (63 nodes, 80 elements)	Quad4-CNS (63 nodes, 40 elements)	Reference [16]
1	872	680	850	825	823
2	5263	4030	5080	4983	4937
3	12,837	10,520	12,830	12,830	12,824
4	14,010	12,810	13,250	13,248	13,005
5	25,816	16,470	23,780	24,394	23,632
6	38,573	18,790	35,780	37,859	36,040
7	40,002	27,820	38,300	38,466	38,442
8	56,043	30,930	48,530	53,295	49,616
9	64,494	36,780	61,530	64,044	63,955
10	73,611	38,090	63,180	70,583	63,967

Table 3
Comparison of computed frequencies (Hz) for the cantilever beam with Mesh C (40×4).

Mode	Quad4 (205 nodes, 160 elements)	NS-FEM-T3 [36] (205 nodes, 320 elements)	ES-FEM-T3 [38] (205 nodes, 320 elements)	Quad4-CNS (205 nodes, 160 elements)	Reference [16]
1	835	780	830	823	823
2	5020	4650	4950	4939	4937
3	12,828	12,200	12,830	12,826	12,824
4	13,264	12,820	13,010	13,019	13,005
5	24,201	16,690	23,550	23,682	23,632
6	37,079	22,010	35,780	36,164	36,040
7	38,480	32,520	38,410	38,451	38,442
8	51,309	33,270	49,030	49,879	49,616
9	64,110	38,340	62,870	63,989	63,955
10	66,508	45,250	63,770	64,452	63,967

of Quad4-CNS element. However, compare to Quad4-CNS element, the Trig6 and Quad8 elements achieve slightly better result. It is noticed that these two elements need adding additional nodes, which increases the size of the global stiffness matrix.

4.3. Cantilever beam for mesh distortion test

The cantilever beam shown in Fig. 2 is also used to investigate the performance of Quad4-CNS element on distorted meshes. As shown in Fig. 7, the cantilever beam is discretized by two elements to investigate the performance of Quad4-CNS, Quad4 and Quad8 elements. The cantilever beam is also discretized into four elements for Trig3 and Trig6 elements. The mesh distortion is controlled by a distortion parameter, $2d/b$, which is a widely used methodology to investigate the sensitivity of numerical methods to distorted meshes [46]. A comparison of computed natural frequency of the first mode is shown in Table 6. A comparison of relative error in the computed frequencies is shown in Fig. 8. Some conclusions can be drawn:

First, the error given by Quad4-CNS element does not change appreciably with the increase in distortion parameters while the error with Trig3, Quad4 and Quad8 elements shows a rapid increase. The present Quad4-CNS element is seen to be almost insensitive to mesh distortion.

Second, the results of Quad4-CNS elements are always much better than those of Trig3 and Quad4 elements.

Third, the results of Quad8 element are better than the numerical results of Trig3, Quad4, and Quad4-CNS elements when the distortion parameter $2d/b$ is smaller than 0.2. However, with the increasing of distortion parameter, accuracy of Quad8 element decreases sharply. When the meshes are severely distorted, the performance of Quad8 element is much worse than that of Quad4-CNS element.

Fourth, compare to Quad4-CNS element, Trig6 element generally achieves more accurate results. However, with the increasing of distortion parameter, accuracy of Trig6 element decreases to the same level as that of Quad4-CNS element. Moreover, as discussed in Section 4.2.2, Trig6 element needs adding additional nodes, which increases the size of the global stiffness matrix.

4.4. A shear wall

Fig. 9 shows a shear wall with four openings [16]. The parameters in the computation are taken as Young's modulus $E=1000$ Pa, Poisson's ratio $\nu=0.2$, thickness $t=1$ m, mass density $\rho=1$ kg/m^3 and plane stress state is assumed. The mesh for computation with 476 elements and 559 nodes is shown in Fig. 10. This problem has earlier been analyzed by Liu and Gu [16] using a local radial point interpolation method (LRPIM) with the multiquadrics (MQ) radial function and by Liu and Nguyen-Thoi using NS-FEM-T3 [36] and ES-FEM-T3 [38]. For reference purposes, the problem has also been solved by them using ANSYS [41] and ABAQUS [16]. Natural frequencies of the first eight modes are

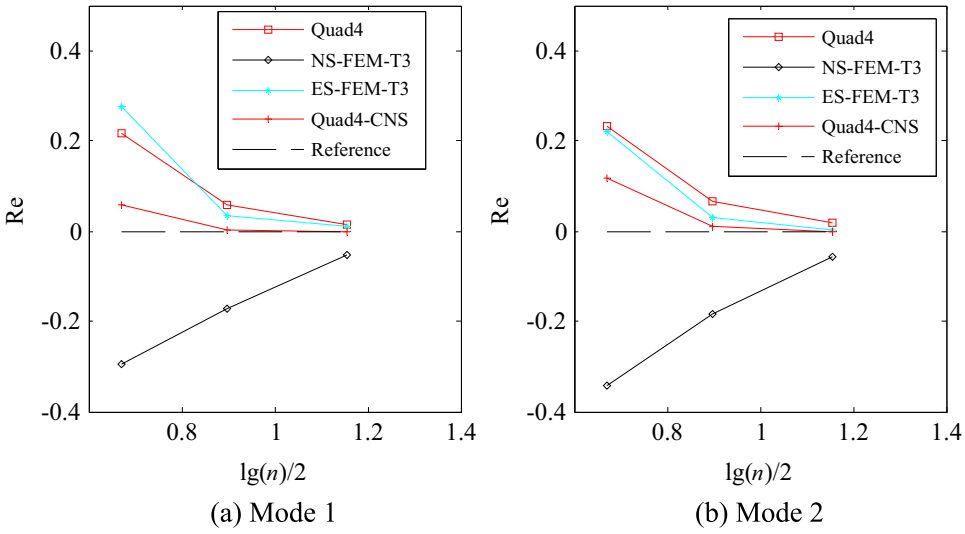

Fig. 4. Convergence of the error in the computed frequency for the first two modes.

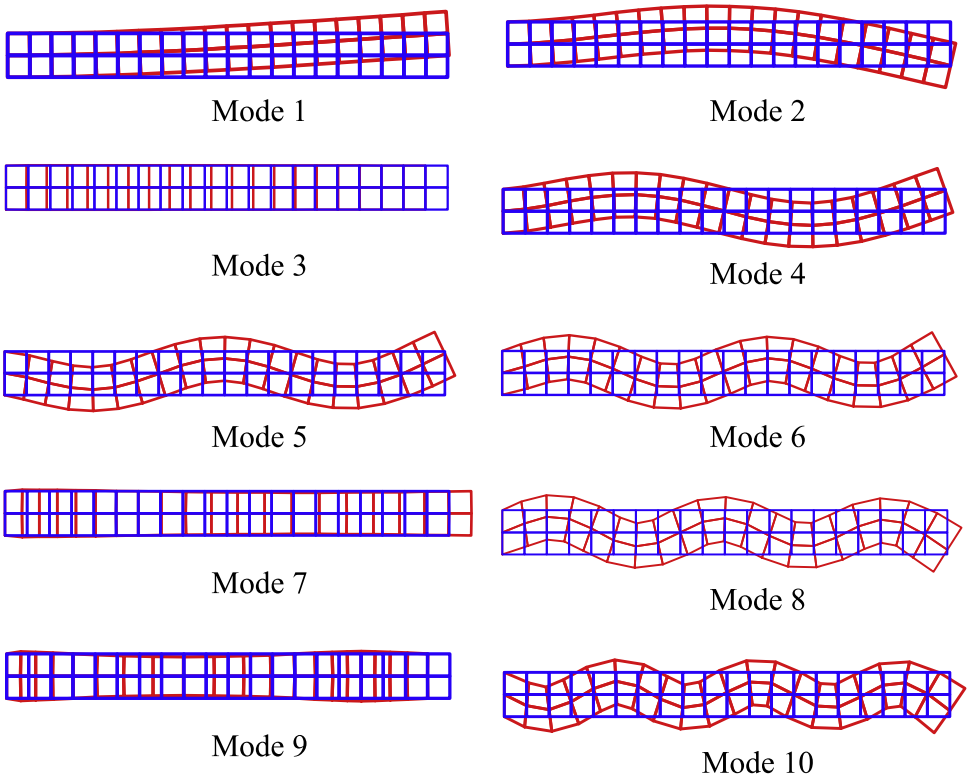

Fig. 5. First to tenth vibration modes of the cantilever beam computed using Quad4-CNS element.

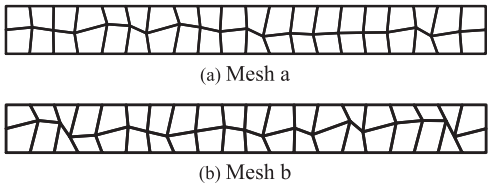

Fig. 6. The distorted grids for the cantilever beam in Fig. 3 (mesh: 20×2).

calculated using the Quad4-CNS element and listed in Table 7. It is seen that the results given by the present Quad4-CNS element are in good agreement with those obtained by other methods. The first to eighth eigenmodes, obtained with the Quad4-CNS element are plotted in Fig. 11. These modeshape plots compare well with that of ES-FEM-T3 [38].

4.5. Slope

In this test, a practical test, homogeneous slope [51], is investigated. This slope is subjected to self-weight, as shown in Fig. 12. This slope is fixed at the bottom. The normal constraints are imposed on the both sides of the slope. The material parameters of this slope are, Young's modulus $E=8\times10^7$ Pa, Poisson's ratio $\nu=0.43$ and unit weight $\gamma=1.962\times10^4$ N/m^3. The mesh for computation with 132 elements and 161 nodes is shown in Fig. 13. Due to the lack of theoretical solution, the mesh in Fig. 13 is refined to obtain a fined mesh with 12,255 elements and 12,528 nodes. A reference solution is calculated by Quad4 element using this fined mesh. Natural frequencies of the first eight modes are calculated using Quad4-CNS element and listed in Table 8. Here again, it is seen that the results given by Quad4-CNS element are better than those obtained by Quad4 element, and comparable to those obtained by Quad8 element. The first 8 eigenmodes, obtained with the Quad4-CNS element are plotted in Fig. 14.

4.6. Forced vibration analysis of a cantilever beam

A benchmark problem of a cantilever beam is investigated using the Quad4-CNS model with the Newmark method for time stepping. The cantilever beam is fixed at the left end with length L and height D, as shown in Fig. 15. It is subjected to a harmonic

Table 4
Comparison of computed frequencies (Hz) for the cantilever beam with distorted grids in Fig. 6. (Mesh a).

Mode	Trig3 (63 nodes, 80 elements)	Trig6 (205 nodes, 80 elements)	Quad4 (63 nodes, 40 elements)	Quad8 (165 nodes, 40 elements)	Quad4-CNS (63 nodes,40 elements)	Reference[16]
1	1139	823	884	823	825	823
2	6727	4942	5325	4940	4986	4937
3	12,851	12,827	12,837	12,827	12,831	12,824
4	17,444	13,034	14,191	13,022	13,254	13,005
5	31,214	23,729	26,131	23,686	24,446	23,632
6	38,636	36,264	38,578	36,158	37,980	36,040
7	47,354	38,454	40,610	38,452	38,467	38,442
8	64,310	50,066	56,747	49,846	53,448	49,616
9	64,900	63,994	64,522	63,991	64,047	63,955
10	82,775	64,758	73,951	64,399	70,639	63,967

Table 5
Comparison of computed frequencies (Hz) for the cantilever beam with distorted grids in Fig. 6. (Mesh b).

Mode	Trig3 (63 nodes, 80 elements)	Trig6 (205 nodes, 80 elements)	Quad4 (63 nodes, 40 elements)	Quad8 (165 nodes, 40 elements)	Quad4-CNS (63 nodes, 40 elements)	Reference [16]
1	1179	823	909	823	826	823
2	6855	4945	5433	4941	4990	4937
3	12,856	12,828	12,838	12,826	12,831	12,824
4	17,845	13,046	14,504	13,028	13,271	13,005
5	31,948	23,760	26,597	23,708	24,480	23,632
6	38,657	36,320	38,584	36,207	38,134	36,040
7	48,668	38,456	41,346	38,452	38,469	38,442
8	64,702	50,155	57,641	49,937	53,761	49,616
9	66,764	63,998	64,546	63,991	64,053	63,955
10	86,403	64,885	76,001	64,499	71,100	63,967

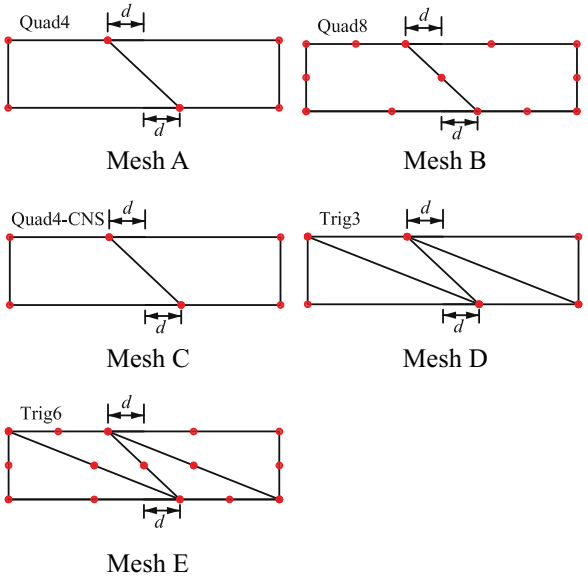

Fig. 7. The mesh used for the distortion sensitivity test.

loading $f(t) = \sin\omega_f t$ in y-direction. The parameters in the computation are taken as $L=4$ m, $D=1$ m, Young's modulus $E=1$ Pa, Poisson's ratio $\nu=0.3$, thickness $t=1$ m, mass density $\rho=1$ kg/m^3, $\omega_f = 0.04$ rad/s, the Rayleigh damping coefficients $\beta_1 = 0.005$, $\beta_2 = 0.272$ and the Newmark method parameters $\alpha = 0.5$, $\delta = 1.0$. The time step $\Delta t = 1.57$ s is used for time integration, while the total computational time is set to be 1200 s.

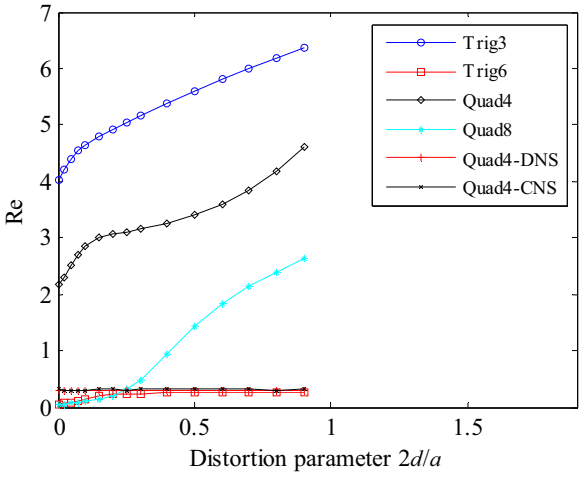

Fig. 8. Error in the computed frequencies of the first mode for distortion sensitivity test.

The domain is represented with 8×2 elements. The problem is also solved with three types of elements including Trig3 (32 elements, 27 nodes), Quad4 (16 elements, 27 nodes), and Quad8 (16 elements, 69 nodes) for the purpose of comparison. Due to the lack of theoretical solution, a very dense quadrilateral mesh with 6400 elements and 6601 nodes is generated. A reference solution is calculated by Quad4 element using this mesh. From the dynamic responses in Fig. 16, it is seen that the amplitudes of the Quad4-CNS element is closer to that of reference solution as compared to the Quad4 element. This shows that the Quad4-CNS element using

Table 6
Computed natural frequencies (Hz) of the first mode for the distortion sensitivity test.

2d/b	Trig3 (6 nodes, 4 elements)	Trig6 (15 nodes, 4 elements)	Quad4 (6 nodes, 2 elements)	Quad8 (13 nodes, 2 elements)	Quad4-CNS[a] (6 nodes, 2 elements)	Reference [16]
0.000	4141	870	2623	869	1093	823
0.025	4297	875	2710	872	1061	823
0.050	4445	890	2889	881	1066	823
0.075	4557	913	3052	894	1070	823
0.100	4642	939	3169	910	1074	823
0.150	4773	983	3296	947	1098	823
0.200	4881	1007	3352	999	1078	823
0.250	4980	1018	3386	1086	1075	823
0.300	5075	1024	3417	1220	1078	823
0.400	5255	1030	3498	1597	1078	823
0.500	5429	1033	3617	1996	1077	823
0.600	5596	1035	3776	2324	1078	823
0.700	5759	1037	3984	2576	1078	823
0.800	5919	1039	4252	2783	1071	823
0.900	6074	1040	4617	2991	1097	823

[a] Six term basis is used.

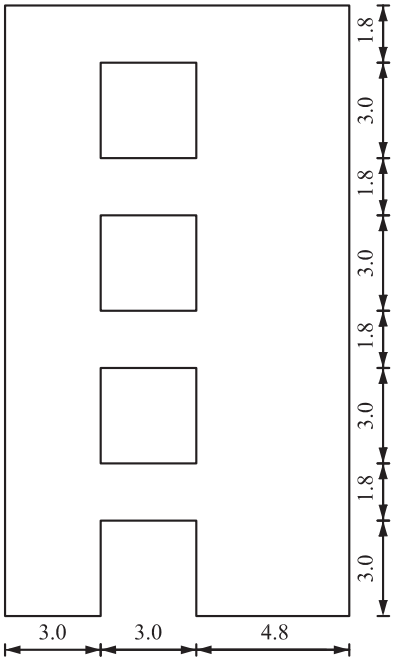

Fig. 9. A shear wall with four openings [16].

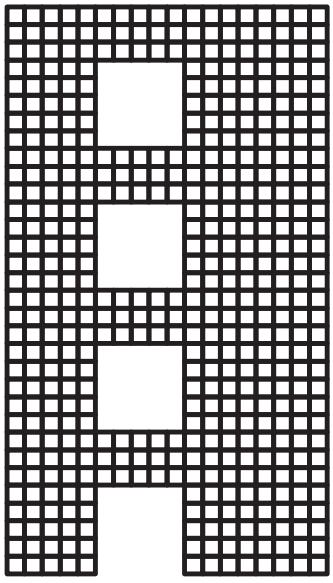

Fig. 10. Model of the shear wall with four openings.

Table 7
Natural frequencies (rad/s) of the shear wall.

Mode	LRPIM (MQ)+ [16]	FEM (ABAQUS) [16]	Brebbia [41,50] BEM	ANSYS Plane 42 with bubble functions [41]	Quad4-CNS
1	2.086	2.073	2.079	2.057	2.094
2	7.152	7.096	7.181	7.067	7.124
3	7.647	7.625	7.644	7.62	7.590
4	12.019	11.938	11.833	11.84	12.192
5	15.628	15.341	15.947	15.313	15.451
6	18.548	18.345	18.644	18.342	18.330
7	20.085	19.876	20.268	19.887	19.858
8	22.564	22.210	22.765	22.236	22.225

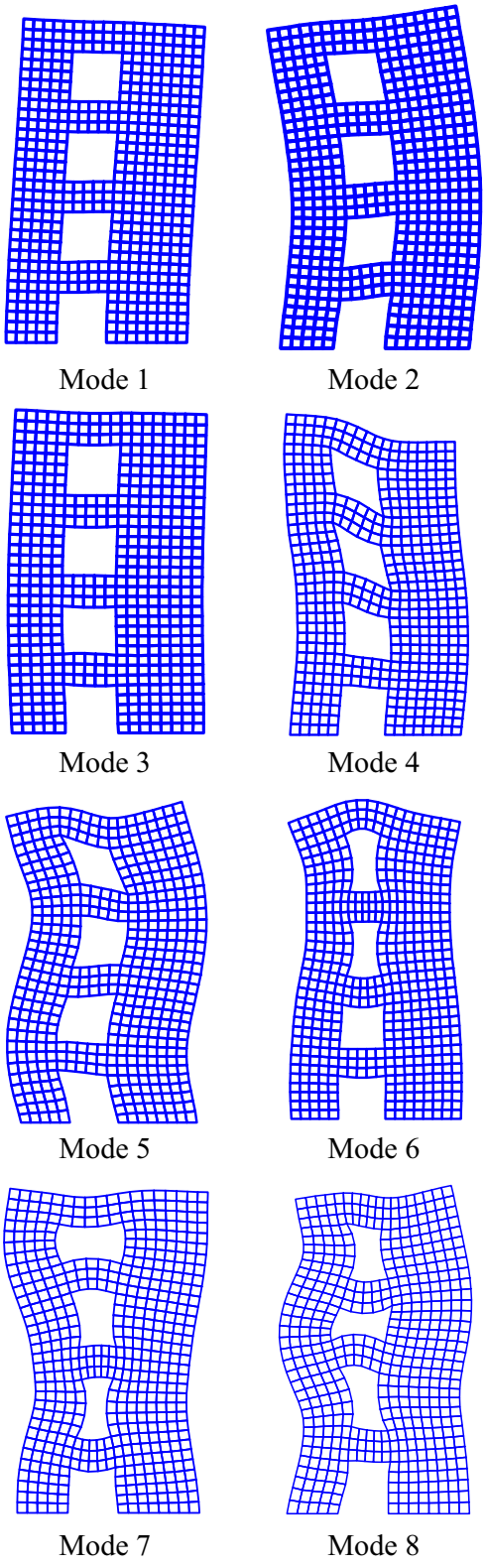

Fig. 11. First to eighth vibration modes of the shear wall with four openings.

quadrilateral mesh can be applied to the forced vibration analysis with excellent accuracy.

5. Discussions and conclusions

In this paper, the PU based quadrilateral element with continuous nodal stress called Quad4-CNS element [43], has been extended to free

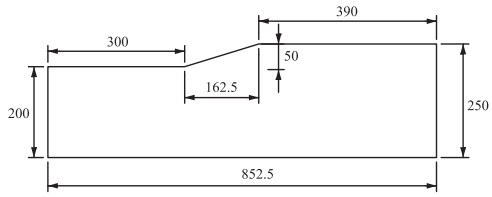

Fig. 12. Dimensions of slope model [51].

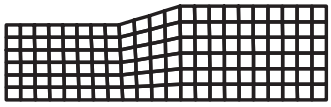

Fig. 13. Discretized model of slope.

Table 8
Natural frequencies (Hz) of the slope.

Mode	Quad4 (161 nodes, 132 elements)	Quad8 (453 nodes, 132 elements)	Quad4-CNS (161 nodes, 132 elements)	Reference
1	0.1799	0.1788	0.1789	0.1789
2	0.2448	0.2395	0.2398	0.2396
3	0.2863	0.2761	0.2770	0.2761
4	0.3134	0.3071	0.3076	0.3072
5	0.3283	0.3133	0.3153	0.3134
6	0.3625	0.3565	0.3572	0.3566
7	0.3821	0.3579	0.3634	0.3579
8	0.3901	0.3825	0.3832	0.3825

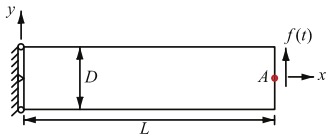

Fig. 15. A 2D cantilever beam subjected to a harmonic loading on the right end.

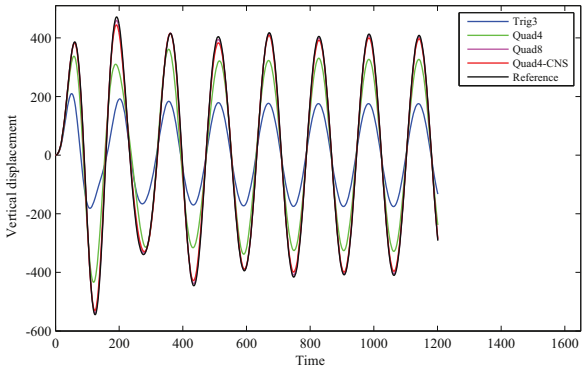

Fig. 16. Transient responses of a cantilever beam subjected to a harmonic loading.

and forced vibration analyses of two-dimensional solids. Some important observations from this work are as follows:

(1) Compared to meshfree methods, the shape functions of Quad4-CNS element possess the much desired Kronecker-delta property, so the essential boundary conditions can be easily applied as in the classical FEM.
(2) Compared to FEM, the Quad4-CNS element does not

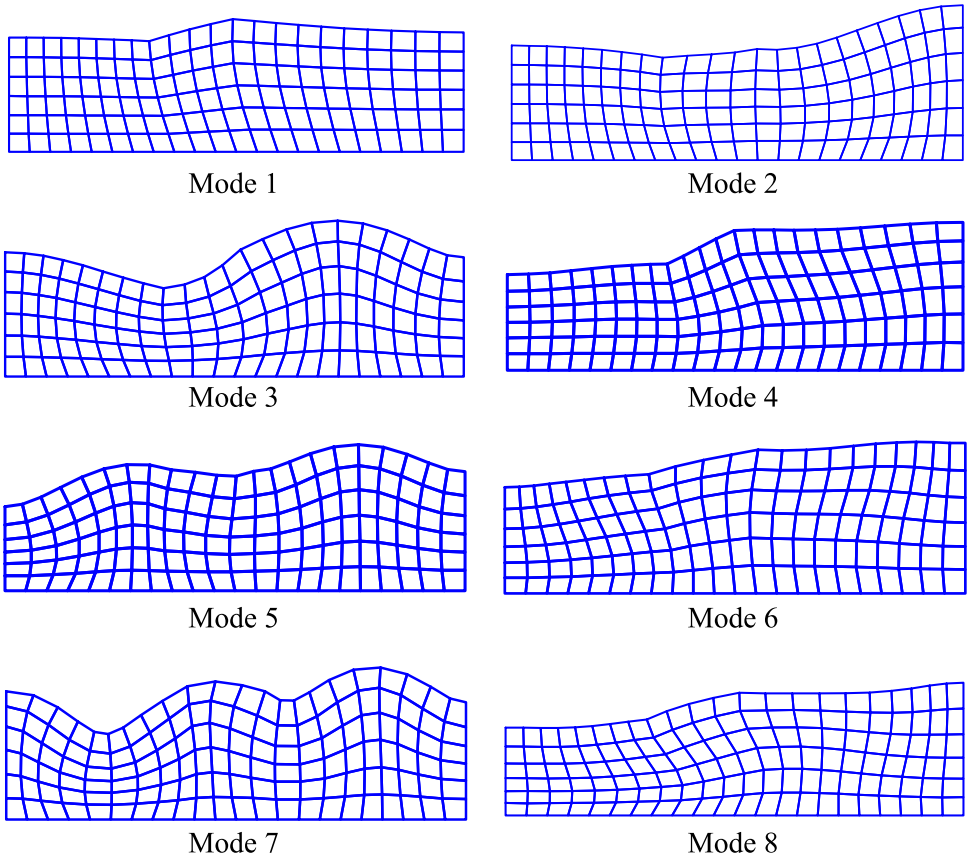

Fig. 14. First to eighth vibration modes of the slope.

necessitate a new mesh or additional nodes in the mesh. It just uses the same mesh as the classical Quad4 element and is able to give more accurate solution than the Quad4 element because a higher order interpolation is used in the Quad4-CNS element.

(3) The linear dependence (LD) problem, which is common in most PU based finite elements, is eliminated automatically in the proposed element. This has been verified by an eigenvalue analysis of the global stiffness matrix before and after applying the boundary conditions [43].

(4) Accuracy of Quad4-CNS element is generally better than that given by Trig3, Quad4, NS-FEM-T3 [36] and ES-FEM-T3 [38] and agrees very well with that of Trig6 and Quad8 elements. The results obtained from the Quad4-CNS element also exhibit a faster convergence than Quad4, NS-FEM-T3 and ES-FEM-T3. Even for the coarse mesh, the results given by Quad4-CNS element are close to the reference solution.

(5) The mesh distortion test conducted shows that the error given by Quad4-CNS element does not change appreciably with the increase in distortion parameters while the error with Trig3, Quad4 and Quad8 shows a rapid increase. Quad4-CNS element is seen to be highly tolerant to mesh distortion.

Acknowlegements

This study is supported by the National Basic Research Program of China (973 Program), under the Grant nos. 2011CB013505 and 2014CB047100; and the National Natural Science Foundation of China, under the Grant no. 11172313.

Appendix A. Features of Quad4-CNS weight functions

The weight functions of Quad4-CNS element have three features:

(1) they satisfy the PUM condition: $\sum_{i=1}^{4} w_i(\xi, \eta) = 1$,

(2) the weight functions satisfy the Kronecker-delta property $w_i(\boldsymbol{x}_j) = \delta_{ij}$ $(i,j=1,2,3,4)$,

(3) Moreover, the gradient of the weight functions is continuous over all the nodes:

$$\left[\frac{\partial w_i\left(\xi_j, \eta_j\right)}{\partial \xi} \frac{\partial w_i\left(\xi_j, \eta_j\right)}{\partial \eta}\right]^T = 0,\ i, j = 1, 2, 3, 4. \tag{B1}$$

Appendix B. Construction of nodal approximation

First the node patch of the node i is defined by Ω_i, as shown in Fig. B1. Here, node i is called central node, and other nodes in domain Ω_i are called satellite nodes. The element support domain $\hat{\Omega}$ is the union of the four node patches $\hat{\Omega} = \cup_{i=1}^{4} \Omega_i$ as shown in Fig. B2.

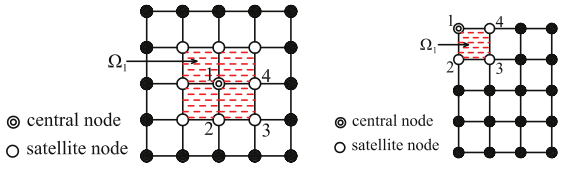

(a) central node within computational domain (b) central node on computational boundary

Fig. B1. The node patch and neighboring elements associated to a central node in the computational domain.

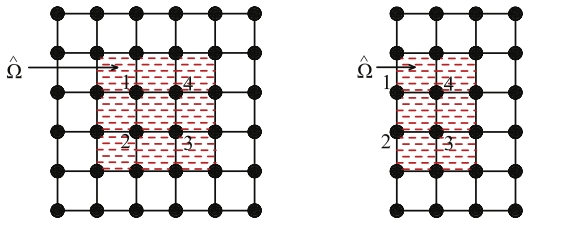

(a) central node within computational domain (b) central node on computational boundary

Fig. B2. Element support domain.

Several constrained least-squares methods have been proposed to construct shape functions with the Kronecker-delta property, such as least square point method (LSPIM) [41], radial point interpolation method (RPIM) [16,47], orthonormalized and constrained moving least-squares method (CO-MLS) [48] and the reduced CO-MLS (CO-LS) [43,44]. Here, the orthonormalized and constrained least-squares method (CO-LS), which is constrained at its central node, is briefly introduced and used to construct the nodal approximation of Quad4-CNS element.

Using least-squares method, the nodal approximation $u_i(\boldsymbol{x})$ can be represented as:

$$u_i(\boldsymbol{x}) = \boldsymbol{p}^T(\boldsymbol{x})\boldsymbol{A}^{-1}\boldsymbol{B}\boldsymbol{a}, \quad \boldsymbol{a} = \left[a_1 a_2 \cdots a_{n^{[i]}}\right]^T, \tag{B2}$$

The moment matrix $\boldsymbol{A}$ and the basis matrix $\boldsymbol{B}$ are expressed as:

$$\boldsymbol{A} = \sum_{j=1}^{n^{[i]}} \boldsymbol{p}(\boldsymbol{x}_j)\boldsymbol{p}^T(\boldsymbol{x}_j), \quad \boldsymbol{B} = \left[\boldsymbol{p}(\boldsymbol{x}_1)\boldsymbol{p}(\boldsymbol{x}_2)\cdots\boldsymbol{p}(\boldsymbol{x}_{n^{[i]}})\right]. \tag{B3}$$

where $n^{[i]}$ is the total number of nodes in the domain Ω_i or the number of supporting nodes for node i, $\boldsymbol{a}$ is a vector of nodal displacements and $\boldsymbol{p}(\boldsymbol{x})$ is a vector of basis functions configured by subsets of the Pascal triangle. In an eight polynomial terms, $\boldsymbol{p}(\boldsymbol{x})$ can be expressed as

$$\boldsymbol{p}(\boldsymbol{x}) = \{1\ x\ y\ x^2\ xy\ y^2\ x^2y\ xy^2\}^T \tag{B4}$$

when considering four or six polynomial terms, $\boldsymbol{p}(\boldsymbol{x})$ are expressed as

$$\boldsymbol{p}(\boldsymbol{x}) = \left\{1\ x\ y\ xy\right\}^T \text{or } \boldsymbol{p}(\boldsymbol{x}) = \left\{1\ x\ y\ x^2\ xy\ y^2\right\}^T \tag{B5}$$

To improve least-squares method, an orthonormalized and constrained least-squares method (CO-LS) is developed using the Gram-Schmidt orthonormalization process [49]. The vector $\boldsymbol{p}$ can be orthogonalized as:

$$\boldsymbol{s} = [s_1 s_2 \cdots s_m]^T = \boldsymbol{R}\boldsymbol{p}, \tag{B6}$$

$\boldsymbol{R}$ is an orthogonalizing matrix with dimension $m \times m$ and m as the number of the monomial terms of $\boldsymbol{p}(\boldsymbol{x})$. The formula of $\boldsymbol{R}$ is presented in reference [48].

Normalizing vector $\boldsymbol{s}$ yields

$$\boldsymbol{r} = \boldsymbol{H}\boldsymbol{p}, \tag{B7}$$

$\boldsymbol{H}$ is an orthonormalizing matrix with dimension $m \times m$ [48].

Using Lagrange multiplier method, the constrained nodal approximation $u_i(\boldsymbol{x})$ can be constructed as

$$u_i(\boldsymbol{x}) = \sum_{j=1}^{n^{[i]}} \hat{\phi}_j^{[i]}(\boldsymbol{x})a_j, \tag{B8}$$

$$\hat{\boldsymbol{\Phi}} = \left[\hat{\phi}_1^{[i]}(\boldsymbol{x}) \hat{\phi}_2^{[i]}(\boldsymbol{x}) \cdots \hat{\phi}_{n^{[i]}}^{[i]}(\boldsymbol{x}) \right]^T = \boldsymbol{r}^T(\boldsymbol{x}) \boldsymbol{B}^{[i]}, \tag{B9}$$

$$\boldsymbol{B}^{[i]} = \left[\boldsymbol{B}_1^{[i]}(\boldsymbol{x}) \boldsymbol{B}_2^{[i]}(\boldsymbol{x}) \cdots \boldsymbol{B}_{n^{[i]}}^{[i]}(\boldsymbol{x}) \right], \tag{B10}$$

$$\boldsymbol{B}_k^{[i]} = \boldsymbol{r}(\boldsymbol{x}_k) - f_k^{[i]} \boldsymbol{r}(\boldsymbol{x}_i) \quad \left(k = 1, 2, \cdots, n^{[i]}\right), \tag{B11}$$

$$f_k^{[i]} = \begin{cases} \sum_{j=1}^{m} (r_{ji} r_{jk}) \Big/ \sum_{j=1}^{m} R_{ji}^2 \quad (k \neq i), \\ \left[\sum_{j=1}^{m} (r_{ji} r_{jk}) - 1 \right] \Big/ \sum_{j=1}^{m} r_{ji}^2 \quad (k = i), \end{cases} \qquad k = 1, 2, \cdots, n^{[i]}. \tag{B12}$$

in which $\hat{\phi}_j^{[i]}(\boldsymbol{x})$ is the shape function of the nodal approximation $u_i(\boldsymbol{x})$ associated with node j.

In defining the support of a given node, the *first order nodal connectivity* which includes the nodes of all the elements connected to the given node is usually considered. Such a support is called *first order support*. However, sometimes, as discussed in [33], the *first order support* may not contain sufficient number of nodes. For example, any of the corner nodes of the mesh in Fig. B1(b) has only four nodes in the first order support. Four nodes are not sufficient to accommodate a quadratic polynomial basis that has six terms in the basis (see Eq. (B5)). At least, six nodes are needed for the purpose. In such cases, a bigger support is defined based on the *second order nodal connectivity* by including the nodes of all the elements connected to the nodes in the *first order support*. Such a support is called *second order support*. Recall that $n^{[i]}$ refers to the total number of nodes in the domain Ω_i or the number of supporting nodes for node i. For the sake of convenience, in the present work, if possible, a support size such that $n^{[i]} > 8$ is usually considered and the number of polynomial terms is chosen to be eight.

References

[1] Zienkiewicz OC, Taylor RL. The finite element method. 5th ed.. . Oxford: Butterworth-Heinemann; 2000.
[2] Paluszny A, Tang XH, Zimmerman RW. Fracture and impulse based finite-discrete element modeling of fragmentation. Comput Mech 2013;52(5):1071–84.
[3] Tang XH, Paluszny A, Zimmerman RW. Energy conservative property of impulse-based methods for collision resolution. Int J Numer Methods Eng 2013;95(6):529–40.
[4] Tang XH, Paluszny A, Zimmerman RW. An impulse-based energy tracking method for collision resolution. Comput Methods Appl Mech Eng 2014;278:160–85.
[5] Lee NS, Bathe KJ. Effects of element distortions on the performance of isoparametric elements. Int J Numer Methods Eng 1993;36(20):3553–76.
[6] Xu JP, Rajendran SA. 'FE-Meshfree' TRIA3 element based on partition of unity for linear and geometry nonlinear analyses. Comput Mech 2013;51(6):843–64.
[7] Calvo B, Martinez MA, Doblare M. On solving large strain hyperelastic problems with the natural element method. Int J Numer Methods Eng 2005;62(2):159–85.
[8] Rabczuk T, Belytschko T. Cracking particles: a simplified mesh-free method for arbitrary evolving cracks. Int J Numer Methods Eng 2004;61(13):2316–43.
[9] Lucy LB. A numerical approach to the testing of the fission thesis. Astron J 1977;82:1013–24.
[10] Nayroles B, Touzot G, Villon P. Generating the finite element method: diffuse approximation and diffuse elements. Comput Mech 1992;10:307–18.
[11] Belytschko T, Lu YY, Gu L. Element-free Galerkin method. Int J Numer Methods Eng 1994;37(2):229–56.
[12] Liu WK, Jun S, Zhang YF. Reproducing kernel particle methods. Int J Numer Methods Eng 1995;20(8–9):1081–106.
[13] Rabczuk T, Belytschko T, Xiao SP. Stable particle methods based on Lagrangian kernels. Comput Methods Appl Mech Eng 2004;193(12-14):1035–63.
[14] Atluri sn, Zhu T. A new meshless local petrov-Galerkin (MLPG) approach in computational mechanics. Comput Mech 1998;22(2):117–27.
[15] Liu GR, Gu YT. A point interpolation method for two dimensional solid. Int J Numer Methods Eng 2001;50(4):937–51.
[16] Liu G, Gu YT. A local radial point interpolation method (LRPIM) for free vibration analyses of 2-d solids. J Sound Vib 2001;246(1):29–46.
[17] Chen L, Nguyen-Xuan X, Nguyen-Thoi T, Zeng KY, Wu SC. Assessment of smoothed point interpolation methods for elastic mechanics. Int J Numer Methods Biomed Eng 2010;89:1635–55.
[18] Rabczuk T, Xiao SP, Sauer M. Coupling of mesh-free methods with finite elements: basic concepts and test results. Commun Numer Methods Eng 2006;22:1031–65.
[19] Babuška I, Melenk JM. The partition of unity method. Int J Numer Methods Eng 1997;40:727–58.
[20] Duarte CA, Babuška I, Oden JT. Generalized finite element methods for three-dimensional structural mechanics problems. Comput Struct 2000;77(2):215–32.
[21] Gross S, Reusken A. An extended pressure finite element space for two-phase incompressible flows with surface tension. J Comput Phys 2007;224(1):40–58.
[22] O'Hara P, Duarte CA, Eason T. Generalized finite element analysis of three-dimensional heat transfer problems exhibiting sharp thermal gradients. Comput Methods Appl Mech Eng 2009;198(21–26):1857–71.
[23] Melenk JM, Babuška I. The partition of unity finite element method: basic theory and applications. Comput Methods Appl Mech Eng 1996;139(1–4):289–314.
[24] Oden JT, Duarte CA, Zienkiewicz OC. A new cloud-based hp-finite element method. Comput Methods Appl Mech Eng 1998;153(1–2):117–26.
[25] Strouboulis T, Babuška I, Copps K. The design and analysis of the Generalized Finite Element Method. Comput Methods Appl Mech Eng 2000;181(1–3):43–69.
[26] Schweitzer MA. Stable enrichment and local preconditioning in the particle-partition of unity method. Numer Math 2011;118(1):137–70.
[27] Zheng H, Liu ZJ, Ge XR. Numerical manifold space of Hermitian form and application to Kirchhoff's thin plate problems. Int J Numer Methods Eng 2013;95:721–39.
[28] Zheng H, Liu F, Li C. Primal mixed solution to unconfined seepage flow in porous media with numerical manifold method. Appl Math Model 2015;39(2):794–808.
[29] Zheng H, Liu F, Li C. The MLS-based numerical manifold method with applications to crack analysis. Int J Fract 2014;190(1–2):147–66.
[30] Zheng H, Xu DD. New strategies for some issues of numerical manifold method in simulation of crack propagation. Int J Numer Methods Eng 2014;97(13):986–1010.
[31] Yang YT, Xu DD, Zheng H. Evaluation on stress intensity factor of crack under dynamic load using numerical manifold method. Chin J Theor Appl Mech 2014;46:730–8.
[32] Belytschko T, Gracie R, Ventura G. A review of extended/generalized finite element methods for material modelling. Model Simul Mater Sci Eng 2009;17(4). http://dx.doi.org/10.1088/0965-0393/17/4/043001.
[33] Xu JP, Rajendran S. A partition-of-unity based 'FE-Meshfree' QUAD4 element with radial-polynomial basis functions for static analyses. Comput Methods Appl Mech Eng 2011;200(47–48):3309–23.
[34] Cai YC, Zhuang XY, Augarde C. A new partition of unity finite element free from linear dependence problem and processing the delta property. Comput Methods Appl Mech Eng 2010;199:1036–43.
[35] Tian R, Yagawa G, Terasaka H. Linear dependence of unity-based generalized FEMs. Comput Methods Appl Mech Eng 2006;195(37–40):4768–82.
[36] Liu GR, Nguyen-Thoi T. Smoothed finite element methods. first edition. USA: CRC Press; 2010.
[37] Nguyen-Xuan H, Rabczuk T, Nguyen-Thoi T, Tran T, Nguyen-Thanh N. Computation of limit and shakedown loads using a node-based smoothed finite element method. Int J Numer Methods Eng 2012;90(3):287–310.
[38] Liu GR, Nguyen-Thoi T, Lam KY. An edge-based smoothed finite element method (ES-FEM) for static, free and forced vibration analyses of solids. J Sound Vib 2009;320(4–5):1100–30.
[39] Nguyen-Thoi T, Liu GR, Vu-Do HC, Nguyen-Xuan H. A face-based smoothed finite element method (fs-fem) for visco-elastoplastic analyses of 3d solids using tetrahedral mesh. Comput Methods Appl Mech Eng 2009;198:3479–98.
[40] Chen JS, Wu CT, Yoon S, You Y. Stabilized conforming nodal integration for galerkin mesh-free methods. Int J Numer Methods Eng 2001;50:435–66.
[41] Zhang BR, Rajendran S. 'FE-meshfree' QUAD4 element for free-vibration analysis. Comput Methods Appl Mech Eng 2008;197(45–48):3595–604.
[42] Yang YT, Tang XH, Zheng H. Construct'FE-Meshfree' Quad4 using mean value coordinates. Eng Anal Bound Elem 2015;59:78–88.
[43] Tang XH, Zheng C, Wu SC, Zhang JH. A novel four-node quadrilateral element with continuous nodal stress. Appl Math Mech (English Edition) 2009;30(12):1519–32.
[44] Yang YT, Tang XH, Zheng H. A three-node triangular element with continuous nodal stress. Comput Struct 2014;141:46–58.
[45] Nagashima T. Node-by-node meshless approach and its application to structural analyses. Int J Numer Methods Eng 1999;46:341–85.
[46] Chen XM, Cen S, Long YQ, Yao ZH. Membrane elements insensitive to distortion using the quadrilateral area coordinate method. Comput Struct 2004;82(1):35–54.
[47] Yang YT, Bi R, Zheng H. A hybrid'FE-Meshless' QUAD4 with continuous nodal stress using radial-polynomial basis functions. Eng Anal Bound Elem 2015;53:73–85.
[48] Zheng C, Tang XH, Zhang JH, Wu SC. A novel mesh-free poly-cell Galerkin method. Acta Mech Sin 2009;25(4):517–27.
[49] Parlett BN. The symmetric eigenvalue problem. USA: Prentice-Hall; 1980.
[50] Brebbia CA, Telles JCF, Wrobel LC. Boundary element techniques.Berlin: Springer-Verlag; 1984.
[51] Guo MW, Li CG, Ge XR, Wang SL, Lu YH. Searching potential slip surface of slopes based on the vector sum analysis method. Rock Soil Mech 2009;30:1775–81.